ACS APPLIED MATERIALS & INTERFACES

Research Article

www.acsami.org

# Targeted Intracellular Controlled Drug Delivery and Tumor Therapy through in Situ Forming Ag Nanogates on Mesoporous Silica Nanocontainers

Changhui Liu,[†,‡] Jing Zheng,[†] Li Deng,[†] Cheng Ma,[†] Jishan Li,[†] Yinhui Li,[†] Sheng Yang,[†,§] Jinfeng Yang,[#] Jing Wang,[#] and Ronghua Yang*[,†,§]

[†]State Key Laboratory of Chemo/Biosensing and Chemometrics, College of Chemistry and Chemical Engineering, Hunan University, Changsha, 410082, P. R. China

[‡]Department of Chemistry and Environmental Engineering, Hunan City University, Yiyang, 413000, P. R. China

[§]School of Chemistry and Biological Engineering, Changsha University of Science and Technology, Changsha, 410004, P. R. China

[#]The Affiliated Cancer Hospital of Xiangya School of Medicine, Central South University, Changsha, 410011, P. R. China

Supporting Information

**ABSTRACT:** Targeting nanocontainers to the pathological zone and controlling release of their cargoes, in particular delivery of anticancer drugs to specific tumor cells in a targeted and controlled manner, remain the key challenges in drug delivery. This paper reports the development of a traceable and tumor-targeted intracellular drug release nanocontainer. The nanocontainer is obtained by in situ growth of silver nanoparticles (AgNPs) on the surfaces of mesoporous silica nanospheres (MSNs) using a DNA-templated process. Additionally, drug release from the nanopores is achieved by selective glutathione (GSH)-triggered dismantle of the AgNPs, and the concurrent fluorescence change allows real-time monitoring of drug release efficacy and facile visualization of in vivo delivery events. After being functionalized with sgc8 aptamer on the outer shell of the AgNPs, the targeted nanocontainers are delivered into acute lymphoblastic leukemia cells by aptamer-mediated recognition and endocytosis. Moreover, the GSH-responsive process presents an improvement in the cell-specific drug release and chemotherapeutic inhibition of tumor growth.

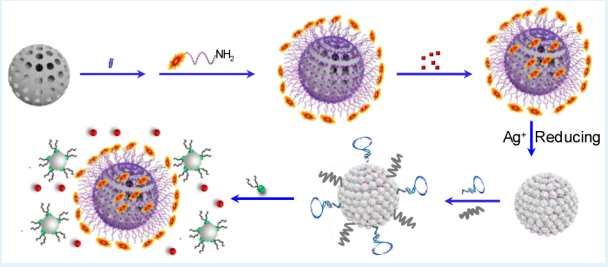


**KEYWORDS:** *drug delivery, mesoporous silica nanoparticle, DNA, silver sphere, glutathione*

## INTRODUCTION

Encapsulation of drugs within nanocontainers that selectively target malignant cells has emerged as a promising tool to improve the pharmacological effect of small-molecule drugs against cancer.[1] To date, MSNs have emerged as robust nanocontainers for drug delivery because of their remarkable biocompatibility and good stability.[2,3] However, the practical application of MSNs in vivo still faces many critical barriers, such as nonspecific drug accumulation at tumor sites and premature release in the circulatory system. For facilitating drug uptake and controlled release, various kinds of nanogates have been fabricated that allow the release of loaded drug molecules into a specific environment in response to external or internal stimuli, such as pH, redox reaction, temperature, and enzymatic activity,[4,5] while such stimuli can be activated in both tumor and normal cells due to the small differences between tumor cells and peripheral normal tissues. To improve targeted delivery, biomarker-targeting ligands have been used to specifically interact with receptors expressed on the cell surface of interest to promote nanocontainers binding and internalization.[6−8] This strategy requires that receptors should be highly overexpressed in cancer cells ($10^4$−$10^5$ copies/cell) relative to normal cells to maximize selectivity and therapeutic efficacy.[9] However, many tumor biomarkers are expressed in both cancer cells and healthy cells, leading to side effects in patients.

Another critical barrier for in vivo application of MSNs is drug leakage during transport in the complex biological environment. The premature release of drug molecules before reaching the target cell not only limits the dose achievement within tumors, but also results in systemic toxicity and undesired side effects. Although poly(ethylene glycol) (PEG) polymers have been known to prolong the circulation time in the bloodstream to improve accumulation at the tumor sites by the enhanced permeation and retention (EPR) effect,[10] PEG functionalization is often not efficient enough to eradicate drug leakage and to exert the anticancer therapy selectively in cancer

Received: February 27, 2015
Accepted: May 13, 2015
Published: May 13, 2015




DOI: 10.1021/acsami.5b01787
ACS Appl. Mater. Interfaces 2015, 7, 11930−11938

cells, because most endogenous stimuli are expressed not only in cytosol, but also in extracellular fluid.

Recognizing these flaws, we report here a new MSNs-based delivery system that allows facile modulation of cell-specific release and tumor therapy by intracellular GSH (Scheme 1).

**Scheme 1. (A) Synthetic Route to the DNA-Guided in Situ Growth of Ag Nanogates on Drug-Loaded MSNs[a]**

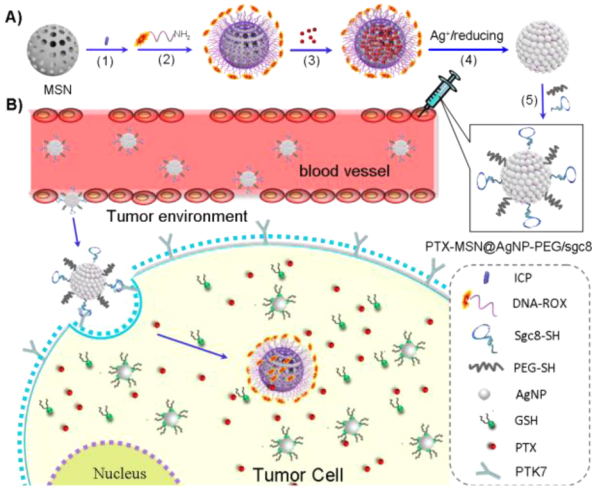


[a]Reaction process: (1) attachment of 3-isocyanatopropyltriethoxysilane; (2) grafting of DNA labeled with 6-carboxylrhodamine (ROX) tag and an amino group; (3) loading of drug molecules; (4) addition of $AgNO_3$, followed by reducing agents; (5) conjugation of aptamer and PEGylation. (B) Schematic illustration of multifunctional PTX-MSNs@AgNPs-PEG/sgc8 for targeted and intracellular GSH-controlled drug delivery and tumor therapy.

GSH, as the most abundant cellular thiol species, plays central roles in many biochemical processes.[11,12] Moreover, while GSH presents low concentration (<10 $\mu$M) in the extracellular fluid, it is relatively concentrated within the cytosol (1−10 mM).[13] In recent years, a range of nanogates have been fabricated and then attached to the surfaces of MSNs through disulfide linkages that are reduced subsequently by antioxidants,[14−17] causing the removal of the nanogates to release the loaded drug molecules. However, the preparation of the nanogates and their capping on MSNs are usually carried out separately, resulting in time-consuming, and technology-intensive. Specially, these systems suffer from undesirable drug leakage, since the antioxidants exist abundantly not only in tumor cells, but also in extracellular compartments. Different from the previous strategies, the nanogates of our MSNs-based delivery system are obtained by in situ growth of AgNPs on MSNs surface through a DNA template-protected process,[18−21] and cargo release from the nanopores is achieved by selective detachment of the AgNPs by GSH-mediated ligand exchange process, that is, a special Ag−S interaction.[18−22] Importantly, through in situ formation, the hybrid AgNPs are easily optimized to ensure drug release triggered only by a high concentration of intracellular GSH and species, as well as lower drug leakage in the biological system. Although significant research progress has been made in developing various functionalized MSNs-based materials for drug delivery and biosensing applications,[3,23,24] several unique functions and features have been incorporated into the present system to deliver drugs in an optimal fashion. First, the DNA strands conjugated on the MSNs' surface act as a "universal molecular glue" to provide a simple and accessible way to cap metal nanostructures, which can be easily modulated to meet different degrees of GSH stimuli. Furthermore, the further functionalization of the outer shell of AgNPs with a tumor-targeting ligand, aptamer sgc8,[25] and the hydrophilic PEG polymer,[9] improves the cancer targeting ability and the long-term stability of the system under physiological conditions. Finally, based on the fluorophore-labeled DNA strand, the emission from the fluorescent tag can be greatly quenched by the formed DNA-templated AgNPs, while the quenched fluorescence would be restored by the GSH-mediated dismantle of AgNPs, thereby providing a simple and facile approach for the visualization of drug delivery/release. The engineering of the MSNs with these functionalities can significantly enhance the therapeutic efficacy and reduce the undesired side effects of the anticancer drug. We also demonstrate that the high drug delivery efficacy of the nanocontainer is attributed to the cooperative effects of aptamer-mediated targeting and intracellular GSH-triggered drug release.

## EXPERIMENTAL SECTION

**Materials.** Sartorius ultrapure water (18.2 MΩ; Millipore Co., Billerica, MA) was used for the preparation of all buffers. *N*-cetyltrimethylammonium bromide (CTAB), tetraethylorthosilicate (TEOS), 3-isocyanatopropyltriethoxysilane (3-ICP), silver nitrate ($AgNO_3$), 2-[4-(2-hydroxyethyl)-1-piperazinyl]ethanesulfonic acid (HEPES), paclitaxel (PTX), glutathione (GSH), and 3-(4,5-dimethylthiazol-2-yl)-5-(3-carboxy-methoxyphenyl)-2-(4-sulfophenyl)-2*H*-tetrazolium (MTS) were purchased from Alfa Aesar Chemical Ltd. All chemicals were of analytical grade and used as received without further purification. The oligonucleotides were synthesized by TaKaRa Biotechnology Co., Ltd., (Dalian, China). The CCRF-CEM cells (T cell line, human acute lymphoblastic leukemia), and Ramos cells (B cell line, human Burkitt's lymphoma) were obtained by the Cell Center of our lab.

**Characterizations.** Transmission electron microscopy (TEM) images were obtained with a JEOL-3010 instrument. Scanning electron microscopy (SEM) images were obtained on a JEOL JSM-6700F microscope. Zeta potential experiments and DLS measurements were performed by ZetaSizer Nanoseries. Fourier transform infrared (FT-IR) spectra were obtained from a TENSOR 27 spectrometer (Bruker Instruments Inc., Germany). UV−vis absorption spectra were collected using a Hitachi U-4100 spectrophotometer (Kyoto, Japan). Small-angle powder X-ray diffraction patterns (XRD) were obtained in a Scintag XDS-2000 powder diffractometer. The nitrogen adsorption−desorption isotherm at 77 K was obtained on a Micromeritics ASAP 2010 Sorptometer by static adsorption procedures. All fluorescence measurements were performed on a PTI QM4 Fluorescence System (Photo Technology International, Birmingham, NJ). Drug concentration was quantified by reversed-phase HPLC (Shimadzu, Japan). Confocal laser scanning microscopy (CLSM) images were obtained on a Fluo View FV 1000 (Olympus, Japan). MTS assay was obtained on a Synergy 2 Multi-Mode Microplate Reader (Bio-Tek, Winooski, TV). Flow cytometric analysis was obtained in a BD FACSCalibur cytometer. In vivo images were acquired using an IVIS Imaging System (Lumina xr).

**Synthesis of MSNs.** CTAB (0.5 g) and sodium hydroxide aqueous solution (1.75 mL, 2.0 M) were dissolved in 240 mL of deionized water, and the solution temperature was adjusted to 353 K. Tetraethoxysilane (TEOS, 2.5 mL) was added dropwise to the surfactant solution under vigorous stirring and aged for 2 h. Then, the solid product was centrifuged, washed with deionized water and ethanol, and dried in air to yield the as-synthesized MSNs. To remove the surfactant template (CTAB), 0.50 g of the as-synthesized MSNs were refluxed for 16 h in a mixture of 2.5 mL of HCl (37.4 wt % in water) and 50 mL of methanol. The resulting material was filtered,


DOI: 10.1021/acsami.5b01787
ACS Appl. Mater. Interfaces 2015, 7, 11930−11938

extensively washed with deionized water and methanol, and dried under high vacuum.

**Synthesis of DNA-Modified MSNs (MSNs-DNA).** One gram of the surfactant-free MSNs was refluxed in 80 mL of anhydrous toluene with 0.25 mL (0.25 g, 1.00 mmol) 3-isocyanatopropyltriethoxysilane (3-ICP) under nitrogen atmosphere for 20 h to immobilize the isocyanate group on the surface. The isocyanatopropyl-functionalized MSNs (MSNs-ICP) was collected and washed with anhydrous toluene three times and dried under vacuum. Next, 100 mg of MSNs-ICP was dispersed in 2.0 mL of deionized water, and the amino-modified oligonucleotides with a concentration of 200 $\mu$M were then added and stirred overnight at room temperature to obtain the DNA-functionalized MSNs (MSNs-DNA). After centrifugation, the absorbance of the supernatant was measured to calculate the amount of DNA attached on the MSNs, which was approximate 5.75 $\mu$mol $g^{-1}$ $SiO_2$.

**Cargo Loading and MSNs Capping.** The purified MSNs-DNA (30 mg) was dispersed in 1.0 mL DMSO solution of paclitaxel (PTX) at room temperature. After stirring for 24 h in dark, the PTX-loaded MSNs-DNA was centrifuged and washed with DMSO, and dried under vacuum. Then, the solid was dispersed in 50 mL PBS (10 mM, pH 7.4) and cooled to 4 °C. An aliquot of $AgNO_3$ solution ($n_{Ag+}$: $n_{DNA}$ = 20:1, 40:1 or 80:1) was then added and stirred for 30 min. Subsequently, HEPES solution (100 mM, pH 7.4) was added as reducing agents for 72 h at 40 °C in dark. The PTX-loaded AgNPs-capped MSNs (PTX-MSNs@AgNPs) were obtained by centrifuging and washing extensively with PBS to remove uncapped drug molecules from the exterior surface of the material. To evaluate the PTX loading amount and efficiency, the supernatant solutions were collected and measured by HPLC (Shimadzu, Japan). The mobile phase consists of acetonitrile/water (70:30 v/v). The quantitative analysis was carried out on a Inertsil ODS-SP. The column temperature is maintained at 30 °C. The flow rate is set at 1.0 mL/min, the detection wavelength was 229 nm, and the sample injection volume was 50 $\mu$L. The loading of PTX was evaluated to be 48 mg $g^{-1}$ $SiO_2$.

**Synthesis of PTX-MSNs@AgNPs-PEG/sgc8.** Before conjugation, thiolated aptamer sgc8 (1.0 mM) was reduced by TCEP (1.0 mM, freshly prepared) in acetate buffer (50 mM, pH 5.2) for 1 h at room temperature. Then, freshly activated aptamer sgc8 (2.0 $\mu$L, 100 $\mu$M) and methoxy-poly(ethylene glycol)-thiol (MW 2000) (2.0 $\mu$L, 100 $\mu$M) were added to the PTX-MSNs@AgNPs suspension (2.0 mL, 1.0 mg $mL^{-1}$) with gentle hand shaking. The mixture was magnetically stirred at room temperature overnight and stored at room temperature for 24 h. After centrifugation at 10,000 rpm for 5 min, PTX-MSNs@AgNPs-PEG/sgc8 hybrids were obtained by drying under high vacuum.

**TEM and SEM Measurements.** TEM measurement was carried out using a JEOL JEM-3010 Ex microscope and HRTEM was measured with a JEOL F-20 microscope. TEM samples were prepared by dropwise adding a solution of redissolved MSNs in DI water on a carbon-coated copper grid. After the solvent evaporated, TEM images were obtained from different spots of each grid. SEM images were obtained on a JEOL JSM-6700F microscope. SEM samples were prepared by dropwise adding a solution of redissolved MSNs in DI water on a silicon wafer. After the solvent evaporated, SEM images were obtained from different spots of each grid.

**Drug Release in Buffer.** A sample of 1.0 mg PTX-MSNs@AgNPs was placed into beakers containing 2.0 mL PBS (10 mM, pH 7.4) and different concentrations of GSH at room temperature under magnetic stirring. At various times, 300 $\mu$L of solution was removed from the beaker and centrifuged at 10,000 rpm for 3 min at 4 °C, followed by measurement of the supernatant by HPLC. The mobile phase consists of acetonitrile/water (70:30 v/v). The quantitative analysis was carried out on a Inertsil ODS-SP. The column temperature is maintained at 30 °C. The flow rate is set at 1.0 mL/min, the detection wavelength was 229 nm, and the sample injection volume was 50 $\mu$L. After that, the nanoparticles were refreshed with fresh buffer for further incubation. The cumulative release (wt %) was calculated as the released quantity of drug divided by the total quantity of loaded nanoparticles.

**Flow Cytometric and Confocal Imaging Analysis.** Cells ($1 \times 10^5$, CEM or Ramos) were treated with PTX-MSNs@AgNPs-PEG/sgc8 or sgc8 in 200 $\mu$L of cell culture medium for 2 h. Afterward, cells were incubated with trypsin for 5 min, washed three times with 200 $\mu$L of washing buffer, suspended in 200 $\mu$L of binding buffer, and subjected to flow cytometry analysis using a BD FACSCalibur cytometer by counting 10 000 events.

CEM ($1 \times 10^5$ cells per well) were pretreated with glutathione monoester (GSH-OEt, 5.0 mM) or *N*-methylmaleimide (NMM, 5.0 mM) in 5% $CO_2$ at 37 °C for 2 h. After washing twice and adding of fresh medium, the cells were incubated with 100 $\mu$g $mL^{-1}$ of PTX-MSNs@AgNPs-PEG/sgc8 for 2 h. The cells were then washed twice with washing buffer and then visualized under a Fluo View FV 1000 (Olympus, Japan). The fluorescence emission spectrum of ROX after being released from MSNs (excitation/emission = 560 nm/610 nm) are detected in the red channel (559 nm/580−640 nm).

**In Vitro Cytotoxicity Assay.** CEM or Ramos cells ($2 \times 10^5$ cells per well) were seeded in 96 well plate. After overnight incubation, the cells were treated with 200 $\mu$L of cell media containing PTX-MSNs@AgNPs-PEG/sgc8 with or without 5.0 mM GSH-OEt, PTX-MSNs@AgNPs-PEG/sgc8 and free PTX (the equivalent dosage of PTX released from PTX-MSNs@AgNPs-PEG/sgc8) for 2 h, respectively. After the medium was removed, 200 $\mu$L of fresh cell medium was added and the 96 well plate was returned to the incubator for another 24 h. Next, the cell culture medium was replaced with 100 $\mu$L of fresh cell medium, followed by the addition of 20 $\mu$L of MTS solution to each well. After incubation for 30 min, the cell viability was determined by a Synergy 2 multi-mode microplate reader (Bio-Tek, Winooski, TV). Each experiment was repeated at least three times, and the error bars represent the standard derivations.

**Animal Culture.** Athymic BALB/c nude mice were purchased from the Changsha SLAC Laboratory Animal Co. Ltd. and maintained under pathogen-free conditions. To establish tumor xenografts, $5 \times 10^6$ in vitro-propagated CEM cells (in 100 $\mu$L of saline) were injected s.c. into the dorsal region of 18−20 g nude mice. All animal operations were performed in accordance with institutional animal use and care regulations, according to protocol No. SYXK (Xiang) 2008−0001, approved by the Laboratory Animal Center of Hunan. Once the tumors had grown to a volume of ~100 $mm^3$, they were ready for the in vivo antitumor efficacy evaluation detailed below. All animals were acclimated to the animal facility for at least 48 h prior to experimentation.

**Specific Uncapping Studies In Vivo.** Before imaging, mice were anesthetized under isoflurane gas (2.0 mL $min^{-1}$) supplemented with oxygen (1.0 mL $min^{-1}$) to be motionless, then a 100 $\mu$L of physiological saline containing PTX-MSNs@AgNPs-PEG/sgc8 or PTX-MSNs@AgNPs-PEG was intravenously (i.v.) injected via the tail vein, and the PTX dosage was kept the same at 1.0 mg $kg^{-1}$. At specified times, fluorescence images of the dorsal region of three mice were taken by a Maestro in vivo fluorescence imaging system. All the fluorescence images were acquired using an IVIS Imaging System (Xenogen).

**In Vivo Anticancer Efficacy Evaluation.** Tumor-bearing mice were randomly assigned to four groups, with four mice in each group treated with saline, free PTX, PTX-MSNs@AgNPs-PEG and PTX-MSNs@AgNPs-PEG/sgc8 with the same dosage of PTX at 1.0 mg $kg^{-1}$ body weight. Drugs were injected through tail veins every other day, and tumor length and width for each mouse were measured by a digital caliper every other day. The tumor volume was calculated using the following equation:

$$\text{tumor volume} = \text{length} \times \text{width}^2/2$$

The body weight of each mouse was also measured every other day to monitor the potential drug toxic side effects. Mice were sacrificed when tumor volume exceeded 4.0 $cm^3$ or at the end of the experiments.

## RESULTS AND DISCUSSION

**Preparation of Drug-Loaded MSNs.** MCM-41 silica nanoparticles were prepared using a surfactant-templated sol−gel process.[26] SEM and TEM micrographs shows the



DOI: 10.1021/acsami.5b01787
ACS Appl. Mater. Interfaces 2015, 7, 11930−11938

constructed MSNs are uniform, monodisperse and spherical in shape with an average diameter of approximately 90 nm and a hexagonally ordered porous array of uniform channel (Figure 1A, B and Supporting Information Figure S1A).[27] MCM-41

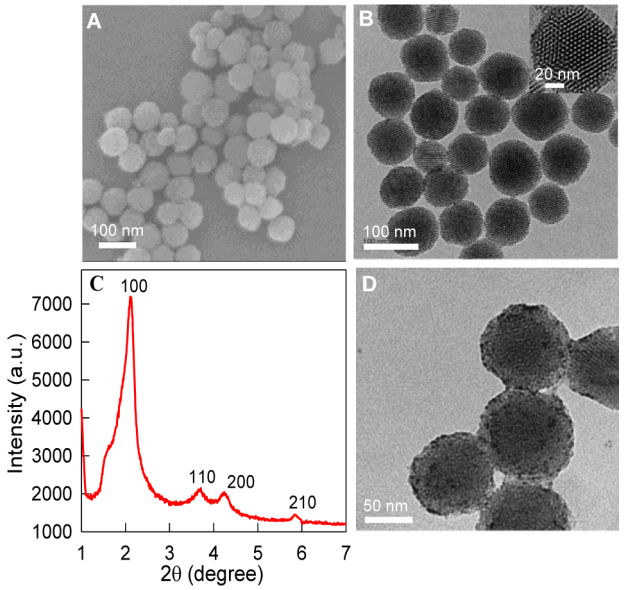


**Figure 1.** (A) SEM image, (B) TEM image and (C) XRD pattern of the MSNs, and (D) TEM image of PTX-MSNs@AgNPs. Inset is the HR-TEM images of MSNs. The concentration ratio of $Ag^+$ to P1 = 40:1.

nanoparticles is further confirmed by the powder XRD pattern (Figure 1C), in which the ratio of the four diffraction peak is approximately $1:\sqrt{3}:2:\sqrt{7}$ in consistent with previous reports.[28−30] To graft DNA strands, the MSNs were first functionalized with isocyanatopropyl groups (ICP) to obtain ICP-functionalized MSNs (MSNs-ICP). After the conjugation, a sharp stretching vibration of the N═C═O group at 2275 $cm^{-1}$ is shown by FT-IR spectroscopy (Supporting Information Figure S2),[31] which proved the successful immobilization of ICP moieties on the MSNs surface. Thereafter, the samples were reacted with a 27-mer single-stranded DNA scaffold,[18,19,32] which was labeled with a 6-carboxylrhodamine (ROX) tag and an amino group (P1, Supporting Information Table S1) to give MSNs-P1 for the formation of DNA-templated AgNPs,[18,33] evidenced by the disappearance of the peak at 2275 $cm^{-1}$ (Supporting Information Figure S2), the decrease of zeta potential from +1.3 mV to −40 mV (Supporting Information Figure S3), and the increase of size distribution (Supporting Information Figure S4). On the basis of all the data, we can conclude that the negatively charged P1 strands had been successfully attached onto the MSNs surface in a covalent manner.

After the drug molecules (paclitaxel, PTX) were loaded into MSNs-P1 cavities (PTX-MSNs-P1), AgNPs were formed by reducing the PTX-MSNs-P1/$Ag^+$ mixture ($n_{Ag+}$: $n_{P1}$ = 40:1) with HEPES buffer, which is a popular pH buffer used extensively in chemical and biochemical experiments and has a mild reducing ability,[34] to obtain PTX-MSNs@AgNPs. As shown in Figure 1D and Supporting Information Figure S5, dark spots on the outside edges of the mesopores can be clearly visualized, representing the aggregation of AgNPs on the exterior surface of MSNs. This event was accompanied by a remarkable increase of zeta potential (Supporting Information Figure S3), and a dramatic decrease of the ROX fluorescence emission (Supporting Information Figure S6), the surface area and pore size distribution during the functionalized process (Supporting Information Figure S7 and Table S2). The presence of AgNPs was also confirmed by EDX analysis (Supporting Information Figure S8), and four distinct diffractions were observed in the high-angle XRD diffraction patterns of PTX-MSNs@AgNPs samples, which were attributed to the diffraction the AgNPs attached to the mesoporous silica nanospheres (Supporting Information Figure S9).[35] In contrast to (MSNs-P1 + $AgNO_3$) with AgNPs capped on the surface of MSNs after reduction, TEM micrographs of the reduction products of mixtures of (MSNs + $AgNO_3$) or (MSNs + P1 + $AgNO_3$) showed that AgNPs were far away from the MSNs surface (Supporting Information Figure S10), indicating the DNA-directed formation of AgNPs on the MSNs surface.

**GSH-triggered PTX Release from PTX-MSNs@AgNPs.** To demonstrate GSH-triggered uncapping of AgNPs from the MSNs surface and the resultant controlled drug release, both the AgNPs absorbance and the ROX fluorescence of PTX-MSNs@AgNPs were examined. As shown in Figure 2A, in phosphate buffered saline solution (PBS, 10 mM, pH 7.4), PTX-MSNs@AgNPs exhibits an electronic transition band

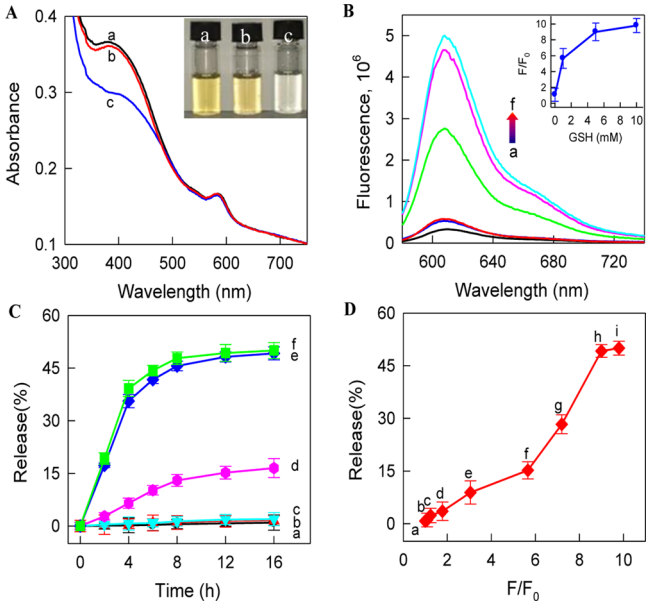


**Figure 2.** (A) UV−visible absorbance spectra of PTX-MSNs@AgNPs in (a) PBS buffer (10 mM, pH 7.4); (b), PBS buffer containing 50% FBS; (c), (b) + 5.0 mM GSH. Inset: the corresponding color of a, b, and c. (B) Fluorescence emission spectra of PTX-MSNs@AgNPs ($\lambda_{ex}$ = 560 nm) upon incubation of (a), PBS buffer; (b), 50% FBS; (c), (b) + 10.0 $\mu$M GSH; (d), (b) + 1.0 mM GSH; (e), (b) + 5.0 mM GSH; and (f), (b) + 10.0 mM GSH after 2.0 h incubation. Inset: fluorescence enhancement of PTX-MSNs@AgNPs in the presence of various GSH concentrations. $F_0$ and $F$ denote ROX fluorescence intensity of PTX-MSNs@AgNsP at 610 nm in 50% FBS without and with GSH, respectively. (C) The corresponding cumulative PTX release from PTX-MSNs@AgNPs in 50% FBS with or without GSH. (D) Correlation between cumulative PTX-release and fluorescence signal of PTX-MSNs@AgNPs after 16 h incubation of different concentrations of GSH (0, 0.01, 0.1, 0.5, 1.0, 2.0, 5.0, and 10 mM from a to (i). $F_0$ and $F$ are ROX fluorescence intensity of PTX-MSNs@AgNsP at 610 nm in 50% FBS without and with GSH, respectively.


DOI: 10.1021/acsami.5b01787
ACS Appl. Mater. Interfaces 2015, 7, 11930−11938

centered at 410 nm, which is attributable to the surface plasmon resonance of AgNPs.[36] Moreover, in the PBS buffer containing 50% fetal bovine serum (FBS, v/v), the absorbance of PTX-MSNs@AgNPs is scarcely influenced, indicating that PTX-MSNs@AgNPs is highly stable in biological environment. However, a quick and dramatic decrease of the AgNPs absorbance is observed in the presence of 5.0 mM GSH in 50% FBS, accompanied by a distinguishable color change (Figure 2A, inset) and the restoration of hexagonally packed mesopores of the MSNs (Supporting Information Figure S11), suggesting that the AgNPs were detached from the MSNs surface. Figure 2B shows the fluorescence emission spectra of PTX-MSNs@AgNPs under different conditions. In 50% FBS, PTX-MSNs@AgNPs is weakly fluorescent due to AgNPs quenching.[18,37,38] However, appreciable emission enhancement is observed as the result of the treatment with GSH, and the intensity increased in a GSH concentration-dependent manner (Figure 2B, inset). Upon addition of 10 $\mu$M GSH, physiologically corresponding to the maximum extracellular GSH concentration level,[13] the ROX fluorescence is slightly increased, while a dramatic increase in ROX fluorescence intensity is observed by 5.0 mM GSH, the intracellular GSH concentration level,[39] suggesting that the bound AgNPs were detached from MSNs through a special Ag−S reaction due to the interaction between template-synthesized AgNPs and DNA is much weaker than that of thiol group and silver.[18−22] This utility was further supported by evaluating the effects of substrates containing different functional groups on the fluorescence of PTX-MSNs@AgNPs. As shown in Supporting Information Figure S12, the sulfhydryl group is the key factor for triggering detachment of AgNPs from the DNA template, thereby forming the basis for constructing the GSH-triggered AgNPs uncapping system proposed in this paper.

Since the detachment of AgNPs from the MSNs is integrated with the uncapping event, in vitro release of PTX with corresponding GSH concentrations was performed by using reversed-phase HPLC analysis.[31,40] In agreement with GSH-induced fluorescence signal enhancement, the data show cumulative release of PTX in a dose-dependent fashion with increasing GSH concentration. In the absence of GSH, little PTX was released into the solution both in PBS and in 50% FBS under stirring for 16 h, signifying the efficient confinement of the drug in the pores of the MSNs by AgNPs capping (Figure 2C). Especially, 10.0 $\mu$M GSH induced a relatively slow release (less than 2% PTX was released over a period of 16 h), while 5.0 mM of GSH led to a burst release of the drug and a maximal cumulative release of ∼50% reached within 12 h. The releasable amount of PTX was consistent with previous reports.[40,41] The PTX release corresponded to the restoration of ROX fluorescence, which could serve as an indicator of drug release. Thus, we evaluated the relationship between the amount of released PTX and the degree of ROX fluorescence enhancement in GSH concentration ranges of 0−1.0 mM or 1.0−10 mM (Figure 2D). Results indicated that the PTX released from the nanocontainer was dependent on the GSH level, meanwhile, the increase in GSH concentration led to a further enhancement of fluorescence signal, proving that the drug delivery system is capable of fluorescent tracking drug release.

Furthermore, because AgNPs capped on the MSNs surface are formed by in situ reduction of the bound $Ag^+$ ions, it is extremely easy to manipulate the concentration of $AgNO_3$ to meet the stimuli of different concentrations of GSH in the various biological environment.[39] To demonstrate these advantages, another two types of AgNPs-capped MSNs with the concentration ratios of $Ag^+$ to P1 of 20:1 and 80:1 were prepared, and GSH-triggered ROX fluorescence recoveries and subsequent PTX releases of three PTX-MSNs@AgNPs systems were determined. Figure 3A shows the ROX fluorescence

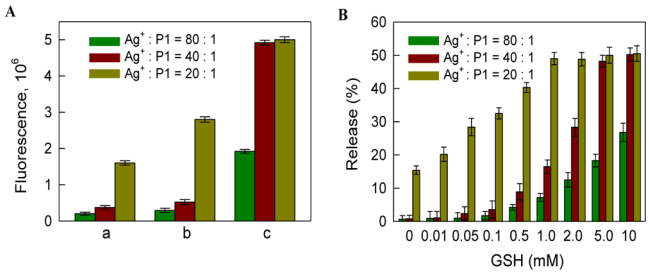


**Figure 3.** Effects of different concentration ratios of $Ag^+$ to P1 of PTX-MSNs@AgNPs on GSH-induced fluorescence restoration and PTX release. (A) Fluorescence intensity changes of PTX-MSNs@AgNP at 610 nm ($\lambda_{ex}$= 560 nm) with various concentration ratios of $Ag^+$ to P1: (a), in PBS buffer; (b), in 50% FBS; and (c), (b) + 5.0 mM GSH at room temperature. (B) The corresponding cumulative PTX-release of the three types of PTX-MSNs@AgNPs systems triggered by different concentrations of GSH at room temperature for 16 h. Data shown represent the mean, with standard deviation, of three separate measurements.

emission changes of the three systems with GSH stimulus. In term of the concentration ratio of $Ag^+$ to P1 to be 20:1, appreciable fluorescence readouts were observed in PBS, and were more prominent in 50% FBS, indicating an undesirable uncapping of the AgNPs. Increasing the ratio of $Ag^+$ to P1 to 40:1 led to negligible changes both in PBS and in 50% FBS in the absence of a trigger, demonstrating good stability in biological environment. After treatment with 5.0 mM of GSH, the fluorescence signal became intensified further, indicating the substantial gate-opening of the nanocontainers. However, further increase of the $Ag^+$ to P1 ratio to 80:1, the system did not give better fluorescence response to GSH than that of $Ag^+$ to P1 of 40:1 under the identical conditions. With the concentration ratios of $Ag^+$ to P1 of 40:1, an almost linear GSH concentration dependence of the fluorescence intensity was observed at 10 $\mu$M < [GSH] < 2.0 mM (Supporting Information Figure S13), which matched quite well with the intracellular relevant concentration of GSH (10 $\mu$M to 10 mM).[13,39,42]

Consistent with GSH-induced fluorescence enhancement, the cumulative PTX release is related to the amounts of $Ag^+$ and P1. Figure 3B shows the cumulative releases in detail of PTX-MSNs@AgNPs triggered by different concentrations of GSH with a fixed stirring time of 16 h at room temperature. At a concentration ratio of $Ag^+$ ions to P1 of 20:1, appreciable release (>20%) of the loaded PTX molecules was observed upon addition of GSH with a concentration of 1.0−10 $\mu$M, which is too low for selective intracellular drug release. Increasing the concentration of $Ag^+$ ions can satisfactorily control release of the loaded PTX molecules. In term of $Ag^+$ ions to P1 of 40:1, < 2% PTX was released at extracellular GSH concentrations over a period of 16 h, yet ∼50% release of the total encapsulated drug molecules was observed in the presence of 5.0 mM GSH. However, with further increase in the amount of $Ag^+$ to 80:1, much higher concentrations of GSH would be needed to remove the capped AgNPs from MSNs, resulting in


DOI: 10.1021/acsami.5b01787
ACS Appl. Mater. Interfaces 2015, 7, 11930−11938

reduced release efficiency. The differences in cumulative release are solely attributed to the AgNPs anchored on the MSNs surface, effectively preventing free elution of the drug, thereby providing the capability for selective controlled drug release. Therefore, this DNA-directed simultaneous synthesis of AgNPs and capping on the MSNs surface provided an efficient and facile route for fabrication of nanogates to avoid premature release and to release drug in a controlled manner. TEM micrographs showed AgNPs can efficiently cap the nanopores with the ratio of $Ag^+$ to P1 of 40:1 (Supporting Information Figure S5), which was employed in the following studies.

**Specific Recognition and Endocytosis.** Sgc8 is an active tumor-targeting ligand that can bind a cancer cell membrane receptor, such as protein tyrosine kinase-7 (PTK7), which is closely associated with CCRF-CEM cells (CEM cells).[21] To develop a targeted and controlled drug delivery system, aptamer sgc8 was linked to the AgNPs surface of PTX-MSNs@AgNPs by a silver-thiol linkage to yield PTX-MSNs@AgNPs-sgc8. Moreover, to avoid the systemic clearance associated with long circulation time,[9,43] PTX-MSNs@AgNPs-sgc8 was further functionalized with methoxy-poly-(ethylene glycol)-thiol (mPEG-SH, 2KD) to obtain a PEGylated nanocontainer, PTX-MSNs@AgNPs-PEG/sgc8. Compared to PTX-MSNs@AgNPs, PTX-MSNs@AgNPs-PEG/sgc8 showed an increase in both zeta potential and average hydrodynamic diameter (Supporting Information Figure S14), and exhibited improved stability in physiological environment (Supporting Information Figure S15). To evaluate the targeting efficiency and specificity of PTX-MSNs@AgNPs-PEG/sgc8, flow cytometry assay and confocal laser scanning microscopy (CLSM) were performed by determining the fluorescence of the labeled ROX. Since sgc8 can specifically bind to PTK7 with high affinity and selectivity, CEM cell with high PTK7 expression was chosen as target cancer cell, whereas Ramos cell without PTK7 on the cell membrane was used as control.[21,44,45] As shown in Figure 4A, CEM cells treated with PTX-MSNs@AgNPs-PEG/sgc8 present a higher fluorescence signal than PTK7-negative Ramos cells (Figure 4B). These results proved that the uptake of PTX-MSNs@AgNPs-PEG/sgc8 is mainly induced by the specific interaction between sgc8 and PTK7. The targeting specificity of sgc8 toward CEM was further confirmed by flow cytometry analysis, as shown in Figure 4C, 4D. To provide the binding specificity of PTX-MSNs@AgNPs-PEG/sgc8, random DNA (Supporting Information Table S1) was anchored onto the surfaces of AgNPs to yield PTX-MSNs@AgNPs-PEG/random DNA. Compared to PTX-MSNs@AgNPs-PEG/random DNA, PTX-MSNs@AgNPs-PEG/sgc8 exhibited a stronger binding affinity to CEM cells, while both of them present much less binding ability toward Ramos cells evidenced by only small fluorescence peak shifts. These corroborating results clearly indicated that PTK7-mediated PTX-MSNs@AgNPs-PEG/sgc8 can selectively recognize and internalize into target CEM cells. Supporting Information Figure S16 shows that most of the nanoparticles are located in the endosome/lysosome judged by the yellow fluorescence.

**Intracellular GSH-Controlled PTX Release.** To investigate that the PTX release from PTX-MSNs@AgNPs-PEG/sgc8 was effectively induced by intracellular GSH, CLSM was used to further confirm the GSH-dependent drug release. A GSH synthesis enhancer (glutathione monoester (GSH-OEt))[46] and GSH scavenger (*N*-methylmaleimide (NMM))[47] were used as modulators to up-regulate and down-regulate the

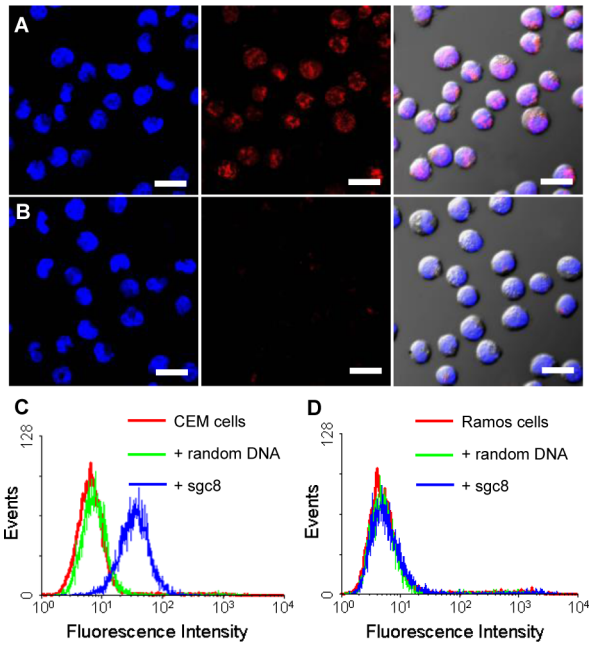


**Figure 4.** Confocal microscopy images of target CEM cells (A) and nontarget Ramos cells (B) treated with PTX-MSNs@AgNPs-PEG/sgc8. Flow cytometry results of CEM cells (C) and Ramos cells (D) after treatment with PTX-MSNs@AgNPs-PEG/sgc8 and PTX-MSNs@AgNPs-PEG/random DNA for 2 h at 37 °C, respectively. The red pseudo color represents the ROX released triggered by GSH, and cell nuclei were stained with Hoechest 33342. Scale bar: 20 $\mu$m.

GSH levels in the CEM cells, respectively. As shown in Figure 5A, red fluorescence can be observed clearly within CEM cells after incubation of PTX-MSNs@AgNPs-PEG/sgc8, indicating

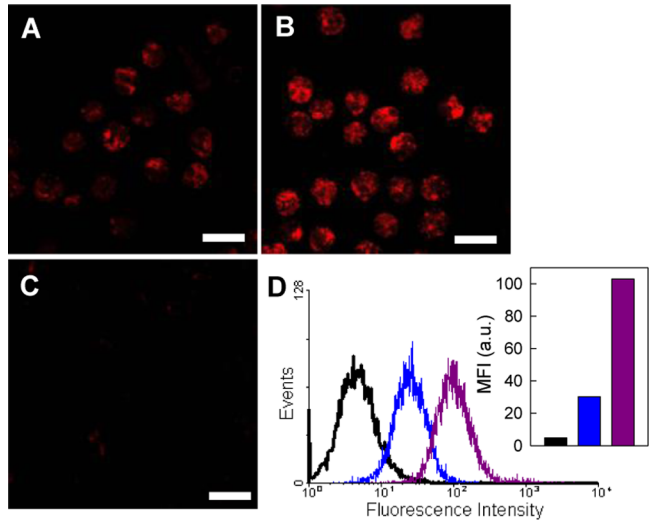


**Figure 5.** Confocal microscopy images of CEM cells treated without GSH-OEt or NMM addition (A), 5.0 mM GSH-OEt (B), and 5.0 mM NMM (C), respectively, followed by incubation with PTX-MSNs@AgNPs-PEG/sgc8. Scale bar is 20 $\mu$m. (D) Flow cytometry analysis of CEM cells treated without GSH-OEt or NMM addition (blue line), with GSH-OEt (red line) and NMM (dark line), respectively, followed by incubation with PTX-MSNs@AgNPs-PEG/sgc8. Inset: the mean fluorescence intensity (MFI) values of A, B, and C. The corresponding pseudobright field images and overlays of the cells with the fluorescence are shown in Supporting Information Figure S17.



DOI: 10.1021/acsami.5b01787
ACS Appl. Mater. Interfaces 2015, 7, 11930−11938

the nanocontainers are taken up by the cells and intracellular GSH induces the removal of AgNPs from the MSNs. Notably, when GSH-OEt was added to elevate the intracellular GSH level, a higher fluorescence signal was observed within CEM cells than the control samples treated without GSH-OEt or NMM addition (Figure 5B and Supporting Information Figure S17), while the fluorescence was markedly weaken upon incubation with NMM (Figure 5C), further indicating that the uncapping of AgNPs was controlled by intracellular GSH levels. Alternatively, flow cytometry assay was used to assess the amount of cellular uptake of PTX-MSNs@AgNPs-PEG/sgc8 quantitatively. In agreement with the results described above, compared with the control cells treated with PTX-MSNs@AgNPs-PEG/sgc8, there were 3.4-fold increases and 4.7-fold decreases of mean fluorescence intensity (MFI) values after treatment with GSH-OEt and NMM, respectively (Figure 5D). Otherwise, a flow cytometry assay was further performed to compare the cell viability in the presence of different GSH levels. Compared with the control samples, remarkably reduced viability of the cells was observed after incubation of GSH-OEt, yet significantly increased after treatment with NMM (Supporting Information Figure S18), suggesting the release of PTX resulted from the particular intracellular GSH stimulus. Taken together, one can easily draw the conclusion that both the synergistic effects of sgc8-mediated uptake of nanocontainers, and intracellular GSH-triggered drug release from PTX-MSNs@AgNPs-PEG/sgc8 enhance the cell killing efficacy of chemotherapeutics.

The in vitro cytotoxicity of PTX-MSNs@AgNPs-PEG/sgc8 against cancer cells was also evaluated by a 3-(4,5-dimethylthiazol-2-yl)-5-(3-carboxymethoxy phenyl)-2-(4-sulfophenyl)-2*H*-tetrazolium (MTS) assay. As shown in Supporting Information Figure S19A, free PTX presents dose-dependent cytotoxicity in both targeted cells and control cells, while PTX-MSNs@AgNPs-PEG/sgc8 present significantly enhanced cytotoxicity toward CEM cells compared with Ramos cells at all the PTX concentrations studied (Supporting Information Figure S19B), suggesting PTX-MSNs@AgNPs-PEG/sgc8 exhibited high cytotoxic activity toward only target cells. Furthermore, neither the blank nanoparticles without PTX (MSNs@AgNPs-PEG/sgc8) nor their released components (i.e., AgNPs) did show inhibitory effect toward CEM cells and Ramos cells (Supporting Information Figure S20), confirming good biocompatibility of our MSNs system. Therefore, it is reasonable to infer that PTX-MSNs@AgNPs-PEG/sgc8 could serve as a promising nanocantainer for targeted therapy.

**Evaluation of in Vivo Antitumor Efficacy.** Following success in the in vitro model, the effectiveness and targeting functions of our nanocontainers was tested in an in vivo model. To demonstrate, the in vivo uncapping of AgNPs from targeted PTX-MSNs@AgNPs-PEG/sgc8 and untargeted PTX-MSNs@AgNPs-PEG administered intravenously into mice bearing CEM tumors was determined by a noninvasive near-infrared optical imaging technique, thus red fluorescent images were obtained. As shown in Figure 6A, the mice treated with PTX-MSNs@AgNPs-PEG/sgc8 present a strong red fluorescence signal mostly in the tumor region. Within 1.0 h postinjection, PTX-MSNs@AgNPs-PEG/sgc8 displays higher fluorescence signal than that of PTX-MSNs@AgNPs-PEG. As time went on, enhanced fluorescence signal of PTX-MSNs@AgNPs-PEG/sgc8 are observed in tumor tissue up to 5 h after injection, while that of PTX-MSNs@AgNPs-PEG is still far too weak (Figure 6B). After 5 h post injection, the mice treated with PTX-

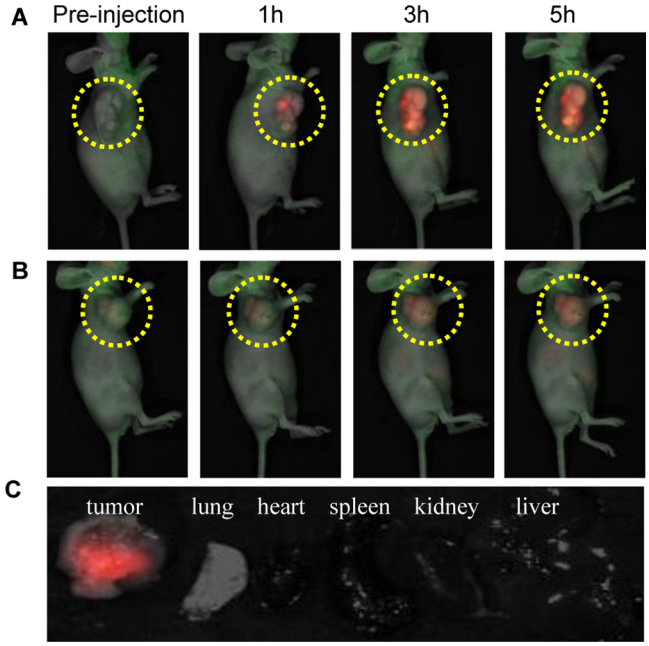


**Figure 6.** Overlaid fluorescent images of CEM-tumor-bearing mice as a function of time after intravenous injection of targeted PTX-MSNs@AgNPs-PEG/sgc8 (A) and untargeted PTX-MSNs@AgNPs-PEG (B) at PTX dosage of 1.0 mg/kg body weight. The tumor sites are marked with dashed yellow circles. (C) Ex vivo fluorescence imaging of the tumor and normal tissues harvested from the euthanized mice bearing CEM tumors at 5 h post injection.

MSNs@AgNPs-PEG/sgc8 were immediately euthanized, and the tumors and major organs including heart, liver, spleen, lung, and kidneys were harvested and analyzed by fluorescence imaging. The red fluorescence signal of the tumors was much higher than that of other normal organs (Figure 6C), suggesting a notable tumor targeting effect and selectively intratumoral gate-opening, thus facile tracking in vivo drug release from GSH-responsive PTX-MSNs@AgNPs-PEG/sgc8.

Next, we evaluated the anticancer therapeutic potency and side effects of antitumor drugs (PTX) delivered by the MSNs system. After the average tumor nodules grew to ~100 $mm^3$, tumor-bearing mice were randomly assigned to four groups, with four mice in each group. Different PTX formulations, such as PTX-MSNs@AgNPs-PEG/sgc8, PTX-MSNs@AgNPs-PEG and free PTX chosen as models, and saline as a negative control were administered by tail vein to mice bearing CEM tumors every other day until the end of the experiments (Figure 7A, B and Supporting Information Figures S21). Both PTX-MSNs@AgNPs-PEG/sgc8 and PTX-MSNs@AgNPs-PEG present remarkably higher tumor suppression than free PTX, suggesting that the MSNs-based delivery system can efficiently delivery PTX inside the tumor, thus leading to enhanced antitumor activity of PTX. More importantly, it was found that a distinct difference in tumor-size inhibition between PTX-MSNs@AgNPs-PEG/sgc8 and PTX-MSNs@AgNPs-PEG, originating from the higher tumor targeting capability of the former than that of the latter. Moreover, in term of toxicity, mice treated with free PTX showed a substantial weight loss, while the weight levels of the other three groups remained relatively unchanged (Figure 7C), indicating that free PTX showed undesirable side effects, whereas others exhibited no obvious adverse effects to the mice in the short term at our tested dose. Taken together, these results demonstrate that not only did


DOI: 10.1021/acsami.5b01787
ACS Appl. Mater. Interfaces 2015, 7, 11930−11938

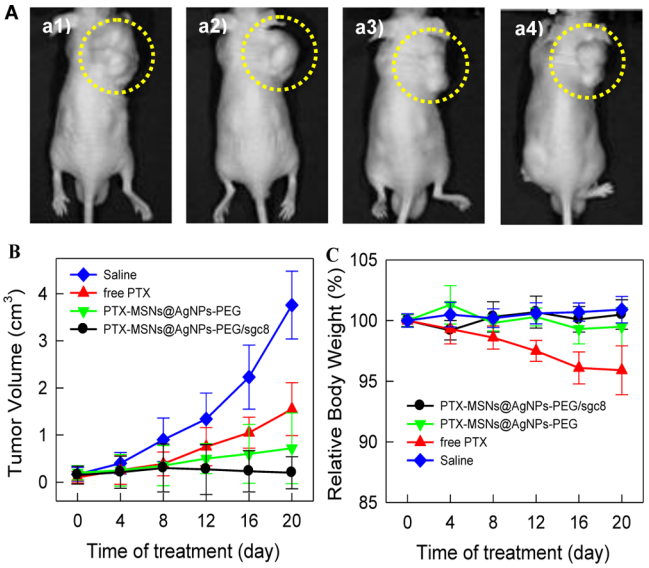


**Figure 7.** Evaluation of in vivo therapeutic efficacy. (A) Representative images of the CEM xenograft tumors of the mice after treatment with saline (a1), free PTX (a2), PTX-MSNs@AgNPs-PEG (a3), and PTX-MSNs@AgNP-PEG/sgc8 (a4) for 20 days. The yellow dashed circles in every image locate the tumor sites and the corresponding images are shown in Supporting Information Figure S17. (B) The CEM tumor volume up to 20 days after treatment with the same dosage of PTX at 1.0 mg $kg^{-1}$ body weight. (C) The body weight variation of CEM tumor-bearing mice during treatment. The average tumor volumes and body weight are shown as means ± the standard deviation ($n$ = 4).

PTX-MSNs@AgNPs-PEG/sgc8 efficiently provide effective intratumoral accumulation and GSH-triggered drug release, but they also mitigate the resultant side effects of PTX, and thereby achieved optimal therapeutic efficacy in vivo.

## CONCLUSIONS

In summary, we have successfully constructed an aptamer-targeted and intracellular GSH-triggered drug release system, which offers capabilities unavailable in conventional drug delivery systems. First, in contrast to conventional covalent or noncovalent strategies, our nanogates are in situ formed and capped on the MSNs surface via a conjugated DNA, thereby providing a less laborious but a more cost-effective and robust approach to constructing AgNPs-coated MSNs. Furthermore, through in situ formation of AgNPs, it is extremely easy to modulate the concentration of $Ag^+$ ions to avoid premature drug release in physiological conditions and to meet GSH stimuli at intracellular concentration but not extracellular levels, a practical demand in clinical applications. Also, the simultaneous synthesis of the gatekeeper AgNPs and capping on MSNs can be easily applied to produce different types of nanogates, including Ag-, Au-, Cu-, Pt-, and Au/Cu/Pt- coated MSNs composites.[48,49] Finally, the drug release from the nanopores of MSNs is determined by a GSH-triggered ligand exchange process. This direct interaction of the trigger with the capped AgNPs enables rapid release of drug molecules without the formation of cellular toxic -SH components,[50] in turn reducing side effects. Meanwhile, the concurrent fluorescence change contributes to facile visualization of the delivery events. We envisioned that our approach will provide a unique methodology for exploitation of high-performance nano-containers for diverse applications in diagnostics, imaging, and drug delivery.

## ASSOCIATED CONTENT

### Supporting Information

More experimental details and spectroscopic data as noted in text. The Supporting Information is available free of charge on the ACS Publications website at DOI: 10.1021/acsami.5b01787.

## AUTHOR INFORMATION

### Corresponding Author

*E-mail: Yangrh@pku.edu.cn. Fax: +86-731-8882 2523.

### Notes

The authors declare no competing financial interest.

## ACKNOWLEDGMENTS

We are grateful for the financial support through the National Natural Science Foundation of China (21405038, 21135001 and 21305036), the Foundation for Innovative Research Groups of NSFC (21221003), the "973" National Key Basic Research Program (2011CB91100-0), and the Fundamental Research Funds for the Central Universities.

## REFERENCES

(1) Yoo, J.-W.; Irvine, D. J.; Discher, D. E.; Mitragotri, S. Bio-inspired, Bioengineered and Biomimetic Drug Delivery Carriers. *Nat. Rev. Drug Discovery* **2011**, *10*, 521−535.

(2) Tran, D.; Ashley, C. E.; Xue, M.; Carnes, E. C.; Zink, J. I.; Brinker, C. J. Mesoporous Silica Nanoparticle Nanocarriers: Biofunctionality and Biocompatibility. *Acc. Chem. Res.* **2013**, *46*, 792−801.

(3) Slowing, I. I.; Trewyn, B. G.; Giri, S.; Lin, V. S. -Y. Mesoporous Silica Nanoparticles for Drug Delivery and Biosensing Applications. *Adv. Funct. Mater.* **2007**, *17*, 1225−1236.

(4) Ambrogio, M. W.; Thomas, C. R.; Zhao, Y.-L.; Zink, J. I.; Stoddart, J. F. Mechanized Silica Nanoparticles: A New Frontier in Theranostic Nanomedicine. *Acc. Chem. Res.* **2011**, *44*, 903−913.

(5) Mura, S.; Nicolas, J.; Couvreur, P. Stimuli-responsive Nanocarriers for Drug Delivery. *Nat. Mater.* **2013**, *12*, 991−1003.

(6) Davis, M. E.; Zuckerman, J. E.; Choi, C. H.; Seligson, D.; Tolcher, A.; Alabi, C. A.; Yen, Y.; Heidel, J. D.; Ribas, A. Evidence of RNAi in Humans from Systemically Administered siRNA Via Targeted Nanoparticles. *Nature* **2010**, *464*, 1067−1070.

(7) Zhang, P.; Cheng, F.; Zhou, R.; Cao, J.; Li, J.; Burda, C.; Min, Q.; Zhu, J.-J. DNA-hybrid-gated Multifunctional Mesoporous Silica Nanocarriers for Dual-targeted and MicroRNA-responsive Controlled Drug Delivery. *Angew. Chem., Int. Ed.* **2014**, *53*, 2371−2375.

(8) Keefe, A. D.; Pai, S.; Ellington, A. Aptamer as Therapertics. *Nat. Rev. Drug Discovery* **2010**, *9*, 537−550.

(9) Peer, D.; Karp, J. M.; Hong, S.; Farokhzad, O. C.; Margalit, R.; Langer, R. Nanocarriers as An Emerging Platform for Cancer Therapy. *Nat. Nanotechnol.* **2007**, *2*, 751−760.

(10) Hubbell, J. A.; Chilkoti, A. Nanomaterials for Drug Delivery. *Science* **2012**, *337*, 303−305.

(11) Meister, A. Glutathione Metabolism and Its Selective Modification. *J. Biol. Chem.* **1988**, *263*, 17205−17208.

(12) Cook, J. A.; Pass, H. I.; Iype, S. N.; Friedman, N.; DeGraff, W.; Russo, A.; Mitchell, J. B. Cellular Glutathione and Thiol Measurements from Surgically Resected Human Lung Tumor and Normal Lung Tissue. *Cancer Res.* **1991**, *51*, 4287−4294.

(13) Santra, S.; Kaittanis, C.; Santiesteban, O. J.; Perez, J. M. Cell-specific, Activatable, and Theranostic Prodrug for Dual-targeted Cancer Imaging and Therapy. *J. Am. Chem. Soc.* **2011**, *133*, 16680−16688.

(14) Cheng, R.; Feng, F.; Meng, F.; Deng, C.; Feijen, J.; Zhong, Z. Glutathione-responsive Nano-vehicles as A Promising Platform for Targeted Intracellular Drug and Gene Delivery. *J. Controlled Release* **2011**, *152*, 2−12.



DOI: 10.1021/acsami.5b01787
*ACS Appl. Mater. Interfaces* 2015, 7, 11930−11938

(15) Giri, S.; Trewyn, B. G.; Stellmaker, M. P.; Lin, V. S. -Y. Stimuli-responsive Controlled-release Delivery System Based on Mesoporous Silica Nanorods Capped with Magnetic Nanoparticles. *Angew. Chem. Int. . Ed.* **2005**, *44*, 5038−5044.
(16) Roggers, R. A.; Lin, V. S. -Y.; Trewyn, B. G. Chemically Reducible Lipid Bilayer Coated Mesoporous Silica Nanoparticles Demonstrating Controlled Release and HeLa and Normal Mouse Liver Cell Biocompatibility and Cellular Internalization. *Mol. Pharmacol.* **2012**, *9*, 2770−2777.
(17) Mortera, R.; Vivero-Escoto, J.; Slowing, I. I.; Garrone, E.; Onida, B.; Lin, V. S. -Y. Cell-induced Intracellular Controlled Release of Membrane Impermeable Cysteine from A Mesoporous Silica Nanoparticle-based Drug Delivery System. *Chem. Commun.* **2009**, 3219−3221.
(18) Jin, J.; Ouyang, X.; Li, J.; Jiang, J.; Wang, H.; Wang, Y.; Yang, R. DNA Template-synthesized Silver Nanoparticles: A New Platform for High-performance Fluorescent Biosensing of Biothiols. *Sci. China Ser. B* **2011**, *54*, 1266−1272.
(19) Petty, J. T.; Zheng, J.; Hud, N. V.; Dickson, R. M. DNA-templated Ag Nanocluster Formation. *J. Am. Chem. Soc.* **2004**, *126*, 5207−5212.
(20) Zinchenko, A. A.; Yoshikawa, K.; Baigl, D. DNA-templated Silver Nanorings. *Adv. Mater.* **2005**, *17*, 2820−2823.
(21) Tao, Y.; Ju, E.; Ren, J.; Qu, X. Metallization of Plasmid DNA for Efficient Gene Delivery. *Chem. Commun.* **2013**, *49*, 9791−9793.
(22) Lin, Y.; Tao, Y.; Pu, F.; Ren, J.; Qu, X. Combination of Graphene Oxide and Thiol-Activated DNA Metallization for Sensitive Fluorescence Turn-On Detection of Cysteine and Their Use for Logic Gate Operations. *Adv. Funct. Mater.* **2011**, *21*, 4565−4572.
(23) Colilla, M.; González, B.; Vallet-Regí, M. Mesoporous Silica Nanoparticles for the Design of Smart Delivery Nanodevices. *Biomater. Sci.* **2013**, *1*, 114−134.
(24) Li, Z.; Barnes, J. C.; Bosoy, A.; Stoddart, J. F.; Zink, J. I. Mesoporous Silica Nanoparticles in Biomedical Applications. *Chem. Soc. Rev.* **2012**, *41*, 2590−2605.
(25) Shangguan, D.; Li, Y.; Tang, Z.; Cao, Z. C.; Chen, H. W.; Mallilaratchy, P.; Sefah, K.; Yang, C. J.; Tan, W. Aptamers Evolved from Live Cells as Effective Molecular Probes for Cancer Study. *Proc. Natl. Acad. Sci. U.S.A.* **2006**, *103*, 11838−11843.
(26) Lai, C.-Y.; Trewyn, B. G.; Jeftinija, D. M.; Jeftinija, K.; Xu, S.; Jeftinija, S.; Lin, V. S. -Y. A Mesoporous Silica Nanosphere-based Carrier System with Chemically Removable CdS Nanoparticle Caps for Stimuli-responsive Controlled Release of Neurotransmitters and Drug Molecules. *J. Am. Chem. Soc.* **2003**, *125*, 4451−4459.
(27) Ahire, J. H.; Chambrier, I.; Mueller, A.; Bao, Y.; Chao, Y. Synthesis of D-Mannose Capped Silicon Nanoparticles and Their Interactions with MCF-7 Human Breast Cancerous Cells. *ACS Appl. Mater. Interfaces* **2013**, *5*, 7384−7391.
(28) Kresge, C. T.; Leonowicz, M. E.; Roth, W. J.; Vartuli, J. C.; Beck, J. S. Ordered Mesoporous Molecular Sieves Synthesized by A Liquid-crystal Template Mechanism. *Nature* **1992**, *359*, 710−712.
(29) Zhang, J.; Yuan, Z. F.; Wang, Y.; Chen, W. H.; Luo, G. F.; Cheng, S. X.; Zhuo, R. X.; Zhang, X. Z. Multifunctional Envelope-type Mesoporous Silica Nanoparticles for Tumor-Triggered Targeting Drug Delivery. *J. Am. Chem. Soc.* **2013**, *135*, 5068−5073.
(30) Wang, C.; Li, Z.; Cao, D.; Zhao, Y. L.; Gaines, J. W.; Bozdemir, O. A.; Ambrogio, M. W.; Frasconi, M.; Botros, Y. Y.; Zink, J. I.; Stoddart, J. F. Stimulated Release of Size-selected Cargos in Succession from Mesoporous Silica Nanoparticles. *Angew. Chem., Int. Ed.* **2011**, *50*, 882−886.
(31) McDonald, A. R.; Dijkstra, H. P.; Suijkerbuijk, B. M. J. M.; Klink, G. P. M. V.; Koten, G. V. Click" Immobilization of Organometallic Pincer Catalysts for C-C Coupling Reactions. *Organometallics* **2009**, *28*, 4689−4699.
(32) Richards, C. I.; Choi, S.; Hsiang, J. C.; Antoku, Y.; Vosch, T.; Bongiorno, A.; Tzeng, Y. L.; Dickson, R. M. Oligonucleotide-stabilized Ag Nanocluster Fluorophores. *J. Am. Chem. Soc.* **2008**, *130*, 5038−5039.
(33) Deng, L.; Ouyang, X.; Jin, J.; Ma, C.; Jiang, Y.; Zheng, J.; Li, J.; Li, Y.; Tan, W.; Yang, R. Exploiting the Higher Specificity of Silver Amalgamation: Selective Detection of Mercury(II) by Forming Ag/Hg Amalgam. *Anal. Chem.* **2013**, *85*, 8594−8600.
(34) Sun, R. W. -Y.; Chen, R.; Chung, N. P. Y.; Ho, C. M.; Lin, C. -L. S.; Che, C.-M. Silver Nanoparticles Fabricated in Hepes Buffer Exhibit Cytoprotective Activities toward HIV-1 Infected Cells. *Chem. Commun.* **2005**, 5059−5061.
(35) Wang, Q.; Yang, X.; Liu, D.; Zhao, J. Fabrication, Characterization and Photocatalytic Properties of Ag Nanoparticles Modified $TiO_2$ NTs. *J. Alloys Compd.* **2012**, *527*, 106−111.
(36) Lee, P. C.; Meisel, D. Adsorption and Surface-enhance Raman of Dye on Silver and Gold Sols. *J. Phys. Chem.* **1982**, *86*, 3391−3395.
(37) Maxwell, D. J.; Taylor, J. R.; Nie, S. Self-assembled Nanoparticle Probes for Recognition and Detection of Biomolecules. *J. Am. Chem. Soc.* **2002**, *124*, 9606−9612.
(38) Li, H.; Rothberg, L. DNA Sequence Detection Using Selective Fluorescence Quenching of Tagged Oligonucleotide Probes by Gold Nanoparticles. *Anal. Chem.* **2004**, *76*, 5414−5417.
(39) Deng, R.; Xie, X.; Vendrell, M.; Chang, Y. T.; Liu, X. Intracellular Glutathione Detection Using $MnO_2$-nanosheet-modified Upconversion Nanoparticles. *J. Am. Chem. Soc.* **2011**, *133*, 20168−20171.
(40) Frasconi, M.; Liu, Z.; Lei, J.; Wu, Y.; Strekalova, E.; Malin, D.; Ambrogio, M. W.; Chen, X.; Botros, Y. Y.; Cryns, V. L.; Sauvage, J.-P.; Stoddart, J. F. Photoexpulsion of Surface-grafted Ruthenium Complexes and Subsequent Release of Cytotoxic Cargos to Cancer Cells from Mesoporous Silica Nanoparticles. *J. Am. Chem. Soc.* **2013**, *135*, 11603−11613.
(41) Li, Z.; Nyalosaso, J. L.; Hwang, A. A.; Ferris, D. P.; Yang, S.; Derrien, G.; Charnay, C.; Durand, J.-O.; Zink, J. I. Measurement of Uptake and Release Capacities of Mesoporous Silica Nanoparticles Enabled by Nanovalve Gates. *J. Phys. Chem. C* **2011**, *115*, 19496−19506.
(42) Verma, A.; Simard, J. M.; Worrall, J. W. E.; Rotello, V. M. Tunable Reactivation of Nanoparticle-inhibited $\beta$-Galactosidase by Glutathione at Intracellular Concentrations. *J. Am. Chem. Soc.* **2004**, *126*, 13987−13991.
(43) Petros, R. A.; DeSimone, J. M. Strategies in the Design of Nanoparticles for Therapeutic Applications. *Nat. Rev. Drug Discovery* **2010**, *9*, 615−627.
(44) Fang, X.; Tan, W. Aptamers Generated from Cell-SELEX for Molecular Medicine: A Chemical Biology Approach. *Acc. Chem. Res.* **2010**, *43*, 48−57.
(45) Zhu, G.; Zheng, J.; Song, E.; Donovan, M.; Zhang, K.; Liu, C.; Tan, W. Self-assembled, Aptamer-tethered DNA Nanotrains for Targeted Transport of Molecular Drugs in Cancer Theranostics. *Proc. Natl. Acad. Sci. U.S.A.* **2013**, *110*, 7998−8003.
(46) Hong, R.; Han, G.; Fernández, J. M.; Kim, B.-J.; Forbes, N. S.; Rotello, V. M. Glutathione-mediated Delivery and Release Using Monolayer Protected Nanoparticle Carriers. *J. Am. Chem. Soc.* **2006**, *128*, 1078−1079.
(47) Kim, H.; Kim, S.; Park, C.; Lee, H.; Park, H. J.; Kim, C. Glutathione-induced Intracellular Release of Guests from Mesoporous Silica Nanocontainers with Cyclodextrin Gatekeepers. *Adv. Mater.* **2010**, *22*, 4280−4283.
(48) Ocsoy, I.; Gulbakan, B.; Chen, T.; Zhu, G.; Chen, Z.; Sari, M. M.; Peng, L.; Xiong, X.; Fang, X.; Tan, W. DNA-guided Metal-nanoparticle Formation on Graphene Oxide Surface. *Adv. Mater.* **2013**, *25*, 2319−2325.
(49) Qing, Z.; He, X.; He, D.; Wang, K.; Xu, F.; Qing, T.; Yang, X. Poly(thymine)-templated Selective Formation of Fluorescent Copper Nanoparticles. *Angew. Chem., Int. Ed.* **2013**, *52*, 9719−9722.
(50) Poon, L.; Zandberg, W.; Hsiao, D.; Erno, Z.; Sen, D.; Gates, B. D.; Branda, N. R. Photothermal Release of Single-stranded DNA from the Surface of Gold Nanoparticles through Controlled Denaturating and Au-S Bond Breaking. *ACS Nano* **2010**, *4*, 6395−6403.


DOI: 10.1021/acsami.5b01787
*ACS Appl. Mater. Interfaces* 2015, 7, 11930−11938